Supplementary Information for

Dual-Band Hydrochromic Optical Modulator for Multimodal Anticounterfeiting and Encryption

Keunhyuk Ryu[a,b], Guanya Wang[b], ZhiLi Dong[a,*], and Yi Long[b,*]

[a] School of Materials Science and Engineering, Nanyang Technological University, 639 798, Singapore.

[b] Department of Electronic Engineering, The Chinese University of Hong Kong, New Territories, 999077, Hong Kong SAR, China.

*Corresponding authors.

E-mail addresses: ylong@ee.cuhk.edu.hk (Y. Long), ZLDong@ntu.edu.sg (Z. L. Dong)

Calculation of transmittance and solar modulation ability according to dry-wet states and humidity

The luminance transmittance (T_{lum}), near-infrared transmittance (T_{NIR}), and solar transm ittance (T_{sol}) were calculated with the formula:

$$T_{lum/NIR/sol} = \frac{\int \varphi_{lum/NIR/sol}\, T(\lambda) d\lambda}{\int \varphi_{lum/NIR/sol} d\lambda}$$

The $T(\lambda)$ is the spectral transmittance (380–780 nm for T_{lum}, 790–2500 nm for T_{NIR}, a nd 360–2500 nm for T_{sol}). $\varphi_{lum}(\lambda)$ is the standard luminous efficiency function of phot opic vision for the wavelength of 380–780 nm.[1] $\varphi_{NIR}(\lambda)$ and $\varphi_{sol}(\lambda)$ are the NIR/solar irradiance spectra for air mass 1.5 (corresponding to the sun standing 37° above the horizon) as wavelength (λ) functions.[1, 2] The visible modulation (ΔT_{lum}), NIR modul ation (ΔT_{NIR}), and solar modulation (ΔT_{sol}) can be calculated by:

$$\Delta T_{lum/NIR/sol} = T_{lum/NIR/sol}\,(Wet) - T_{lum/NIR/sol}\,(Dry)$$

Calculation of MIR emissivity according to dry-wet states and humidity

MIR emissivity modulation ability ($\Delta\varepsilon_{MIR}$) was calculated with the following formula:

$$\Delta\varepsilon_{MIR} = \varepsilon_{MIR-Wet} - \varepsilon_{MIR-Dry}$$

$\varepsilon_{MIR\text{-}Wet}$ refers to the integrated MIR emissivity of the sample measured under wet stat e, and $\varepsilon_{MIR\text{-}Dry}$ refers to the integrated MIR emissivity of the sample measured under dry state. The ε_{MIR} spectral curve was plotted according to Kirchhoff's law of thermal radiation: $\varepsilon(\lambda) = A(\lambda) = 1\text{-}T(\lambda)\text{-}R(\lambda)$.[3, 4] Where $R(\lambda)$ is the spectral MIR reflectance and $T(\lambda)$ is the spectral MIR transmittance measured with a FTIR spectrometer equip

ped with an integrating sphere.

Finite difference time domain (FDTD) simulations detail

Simulated optical properties were calculated using commercial software Ansys Lumeric al FDTD. 3D multilayer models were created by stacking 20 μm-thick porous PMMA, 200 nm-thick ITO, and 40 μm-thick SiO_2 layers. Because PMMA forms the dominan t porous framework after drying and the refractive index (n) difference between PMM A (n ≈ 1.49) and PVP (n ≈ 1.52) is small, a simplified porous PMMA model was a dopted in the FDTD simulation.[5, 6] The optical constants of PMMA, ITO, and glass were obtained from reference.[7, 8] The pores with an average diameter of ~4 μm insid e PMMA were defined as air and water to simulate dry and wet states. Periodic bou ndary conditions were set in the *x*, *y* directions of the simulation region, and perfectl y matched layer boundary conditions were set in the *z* direction. The mesh accuracy l evel was set to 4, and the auto shutoff value was set to 10^{-5}. A plane wave source with fixed wavelength was built above the PMMA layer with the propagation along t he negative *z* direction. Two power monitors were built above light source and below SiO_2 layer to measure reflectance and transmittance. A profile monitor was built on *x*-*z* plane with the position of $y = 0$ to record electric field distribution, and a mesh size of 40 × 40 × 40 nm^3 was overridden on it for high-resolution imaging.

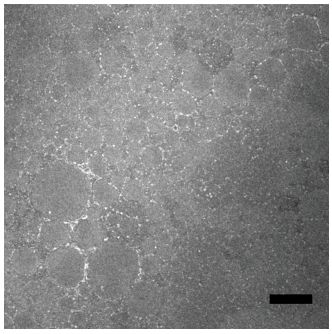

Figure S1. *Microstructure of 0.5 wt% PMMA sample (scale bar: 10 μm).*

Microstructure of the hydrochromic optical modulator according to the PMMA coating layers

Figure S2a shows the microstructural evolution of the hydrochromic optical modulator as a function of the number of PMMA coating layers. The single-layer sample exhibits a highly porous surface with the largest pore area compared to multilayer coatings. As the number of layers increases, the surface pores become increasingly covered, leading to a progressive reduction in the exposed pore area. Eventually, in the case of excessive coating layers, most pores are sealed by the overlying PMMA, resulting in a decrease in pore area. As quantified in Figure S2b, the pore size slightly reduced as the number of coating layers increased. Meanwhile, the pore area exceeds ~60% for the single-layer sample but decreases steadily with additional layers, reaching a minimum of ~20%. Therefore, the single-layer coating was adopted as the optimal coating parameter.

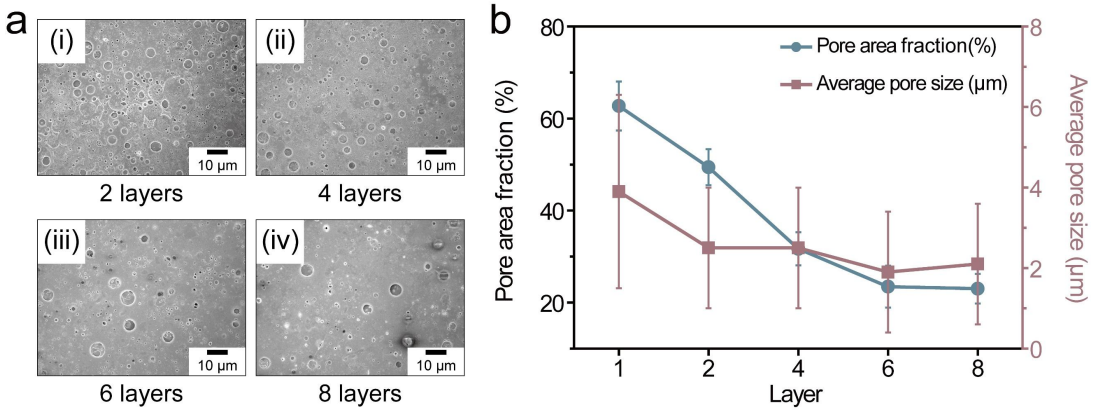

Figure S2. *(a) Porous PMMA microstructures as a function of coating layers: (i) 2 layers, (ii) 4 layers, (iii) 6 layers, and (iv) 8 layers. (b) Pore area and pore size of porous PMMA as a function of coating layers.*

Response speed of the hydrochromic modulator

As shown in Figure S3, the hydrochromic modulator was first immersed in water for 1 min to reach the fully wetted state and subsequently dried at 80 °C while monitoring the temporal evolution of optical transmittance and emissivity. In the wet state, the device exhibited a high T_{lum} of approximately 75% and a high ε_{MIR} of approximately 0.85. During drying, both values gradually decreased, reaching below 15% for T_{lum} and approximately 0.2 for ε_{MIR} after 160 seconds. These results demonstrate that the dual-band optical device enables synchronized

and reversible modulation of visible transmittance and mid-infrared emissivity with a relatively fast response under thermal drying conditions.

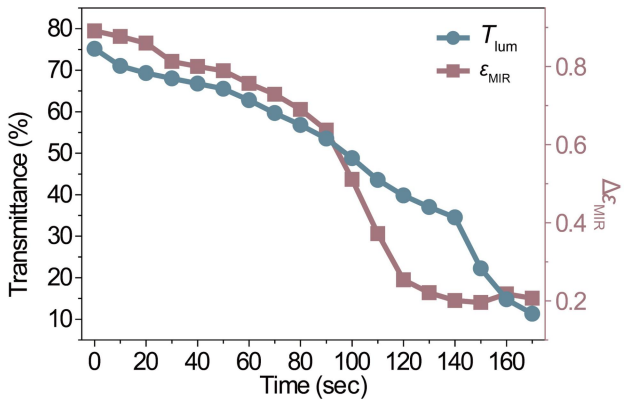

Figure S3. *Optical transmittance and emissivity response speed.*

Optical modulation performance of hydrochromic modulators as a function of spin-coating speed (rpm)

As shown in Figure S4, the optical modulation performance gradually increases with spin speed, reaching a maximum of nearly 50% at 500 rpm. However, a further increase to 600 rpm results in a decline in modulation performance. This behavior is attributed to the reduced thickness of the hydrochromic layer at higher spin speeds, which leads to elevated baseline transmittance even in the dry state, thereby diminishing the overall modulation contrast. Therefore, a spin speed of 500 rpm was adopted as the optimal coating parameter.

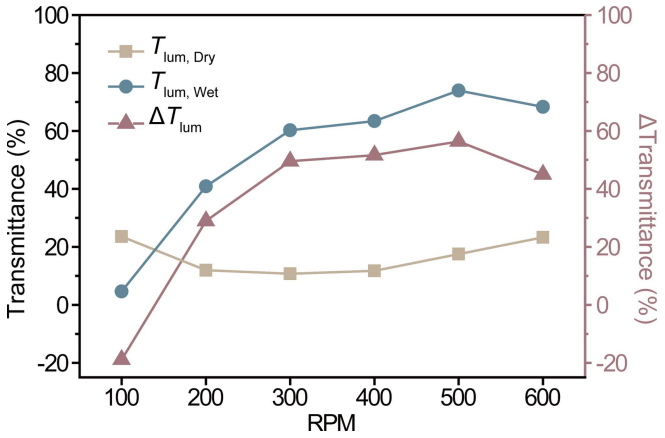

Figure S4. *Optical transmittance characteristics measured with a point detector as a function of coating speed.*

Optical performance of the hydrochromic optical modulator according to PMMA concentration and coating layers

Figure S5a illustrates the hydrochromic performance as a function of PMMA concentration. Samples with PMMA concentrations up to 2 wt% exhibit limited modulation performance, with ΔT_{lum} and ΔT_{sol} both below ~25%. In contrast, the 4 wt% sample achieves the highest modulation values, peaking at approximately 50% for both ΔT_{lum} and ΔT_{sol}. Beyond 6 wt%, the modulation performance declines, presumably due to the reduction in pore size and pore area. As shown in Figure S5b, the sample with a single 4 wt% PMMA layer exhibits the highest modulation performance. Specifically, it achieves ΔT_{lum} and ΔT_{sol} values of 56% and 55% (Figure S5b). However, as the number of layers increases, the modulation performance decreases, reaching minimum values of 33% for ΔT_{lum} and 32% for ΔT_{sol}. This reduction is likely due to a decrease in effective pore area, as additional layers partially cover or fill the surface pores, thereby diminishing the modulation capability. Therefore, the single 4 wt% PMMA layer was adopted as the optimal coating parameter.

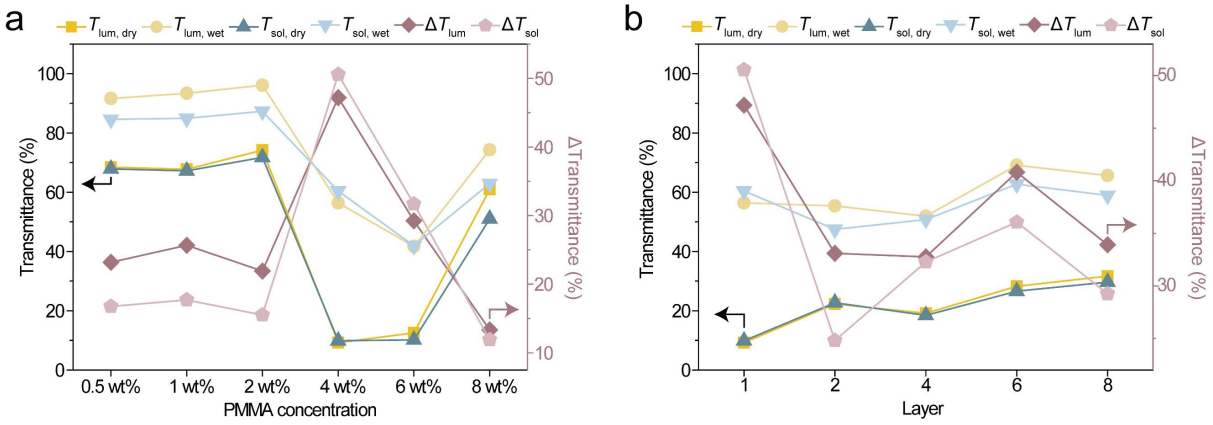

Figure S5. *Optical transmittance characteristics as a function of (a) PMMA concentration and (b) coating layer.*

Overall optical and $\Delta\varepsilon_{MIR}$ properties of dual-band optical modulator according to PMMA concentrations and coating layers.

Figure S6 shows the overall ΔT_{lum}, ΔT_{sol}, and $\Delta\varepsilon_{MIR}$ characteristics of the hydrochromic optical modulator, as a function of PMMA concentration and coating layers. As shown in Figure S6a, PMMA concentrations up to 2 wt% exhibit limited optical modulation ($\Delta T_{lum/sol}$ < ~25%). A significant increase is observed at 4 wt%, where ΔT_{lum} and ΔT_{sol} exceed ~50%. However, at 6 and 8 wt%, the modulation decreases again, with $\Delta T_{lum/sol}$ falling below a minimum of ~15%. The ε_{MIR} modulation remains high (~0.65) up to 2 wt%, but gradually decreases beyond 4 wt%, reaching a minimum value of 0.4 at 8 wt%. Figure S6b reveals that both $\Delta T_{lum/sol}$ and $\Delta\varepsilon_{MIR}$ progressively decline with increasing coating layers. The single-layer sample exhibits the highest modulation performance ($\Delta T_{lum/sol}$ > 50%, $\Delta\varepsilon_{MIR}$ = 0.55), while the 8-layer sample shows the lowest values ($\Delta T_{lum/sol}$ < 33%, $\Delta\varepsilon_{MIR}$ = 0.31). Based on these results, the optimal coating condition for balancing visible and infrared modulation performance was determined to be a PMMA concentration of 4 wt% with a single-layer structure (ΔT_{lum} = 47%, ΔT_{sol} = 50%, $\Delta\varepsilon_{MIR}$ = 0.55).

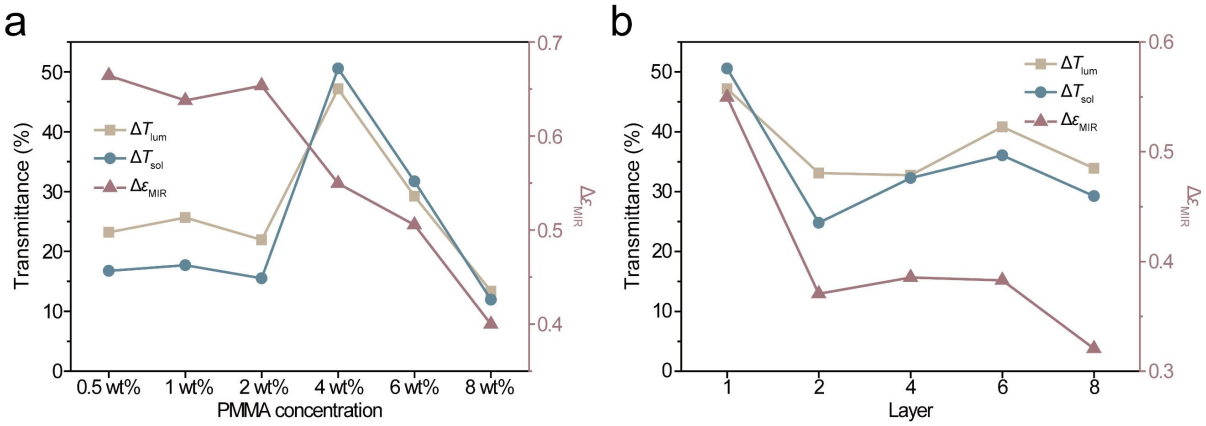

Figure S6. *Overall optical transmittance and emissivity modulation performance: (a) function of PMMA concentration and (b) coating layer.*

Overall optical modulation properties of dual-band optical modulator according to humidity variations.

Figure S7a illustrates the visible-range transmittance modulation behavior of the sampl e as RH increases from 50% to 85%. The transmittance remains low (~20%) at 50%

RH and progressively increases with rising humidity, reaching approximately 60% at 85% RH. As demonstrated in Figure S7b, this modulation shows a strong linear correlation with RH, evidenced by a high coefficient of determination (R^2 = 0.99), confirming the sample's excellent sensitivity to humidity. Furthermore, the sample maintains stable and repeatable transmittance values at each RH level across 20 cycles, verifying consistent humidity-responsive optical performance (Figure S7c). In addition to visible transmittance modulation, the sample also exhibits ε_{MIR} modulation response to humidity changes. As shown in Figure S7d, the sample displays a low emissivity of approximately 0.2 at 50% RH, gradually increasing with humidity to a peak value of 0.71 at 85% RH. The ε_{MIR} modulation behavior also shows a reliable linear relationship with RH, achieving a high coefficient of determination (R^2 = 0.98), further highlighting the sample's sensitivity to humidity (Figure S7e). Moreover, Figure S7f demonstrates that the ε_{MIR} values at each RH level are consistently stable and repeatable across 20 humidity cycles, confirming the reliable humidity-dependent emissivity modulation. Collectively, these results indicate the sample's promising dual-band modulation capabilities, responsive not only to direct water exposure but also exhibiting precise and stable responses to incremental humidity variations.

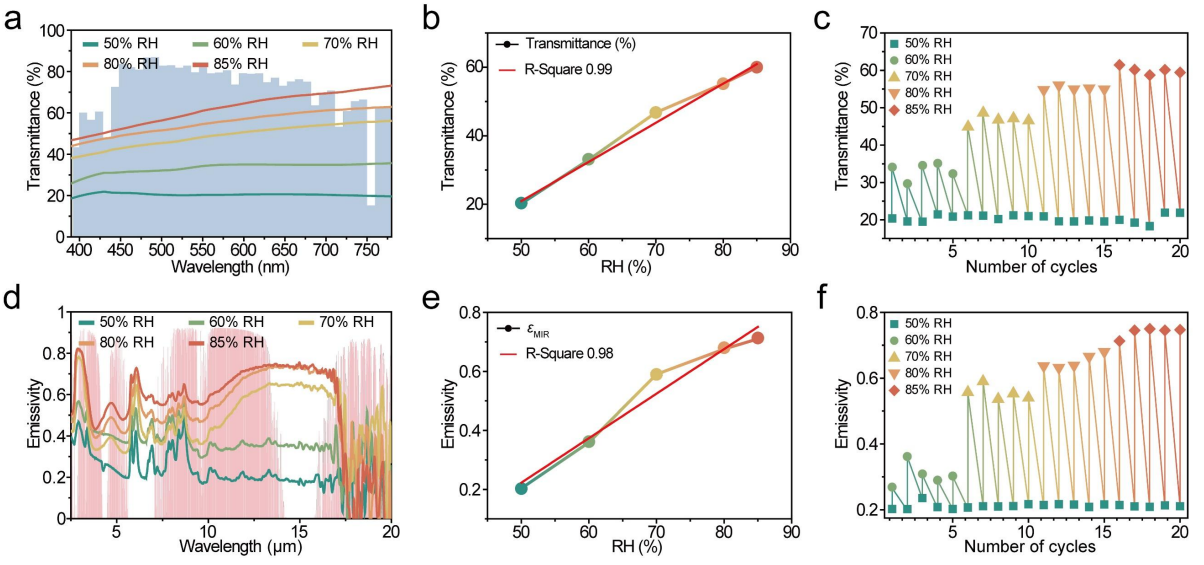

Figure S7. *(a) Visible transmittance spectra under various RH levels, overlaid with a normalized AM1.5 global solar spectrum (blue-shaded area). (b) Optical transmittance as a function of relative humidity. (c) T_{lum} modulation behavior under repeated RH exposures at different humidity levels. (d) Emissivity spectra at different RH levels, shown alongside the normalized A*

M1.5 atmospheric transmittance spectrum (red-shaded area). (e) Average emissivity values under varying relative humidity conditions. (f) ε_{MIR} modulation behavior under repeated RH exposures at different humidity levels.

Optical modulation properties of the control group and the prototype.

Figure S8 compares the optical properties of the control group and the prototype, highlighting the critical role of dual-band modulation. The control group exhibits a pronounced luminance transmittance contrast between the dry and wet states, with T_{lum} increasing from 24.5% (dry) to 65.5% (wet), as shown in Figure S8a. However, owing to the absence of the low-E layer, the near-infrared and solar transmittance contrasts remain relatively limited compared to those of the prototype, with T_{NIR} values of 42.5% and 74.9% and T_{sol} values of 32.6% and 69.2% in the dry and wet states, respectively. More importantly, the ε_{MIR} difference between the dry and wet states is negligible, with $\Delta\varepsilon_{MIR}$ below 0.1. By contrast, the prototype exhibits pronounced modulation across all key optical and thermal parameters, including T_{lum}, T_{NIR}, T_{sol}, and ε_{MIR}, as a direct result of its dual-band modulation capability (Figure S8b). In the dry state, the prototype shows transmittance values below ~10% across the visible, NIR, and solar ranges, together with a low ε_{MIR} of ~0.4. Upon wetting, both transmittance and ε_{MIR} increase markedly, yielding transmittance contrasts of approximately 50% in T_{lum}, T_{NIR}, and T_{sol}, as well as a large emissivity modulation of $\Delta\varepsilon_{MIR} \approx 0.5$.

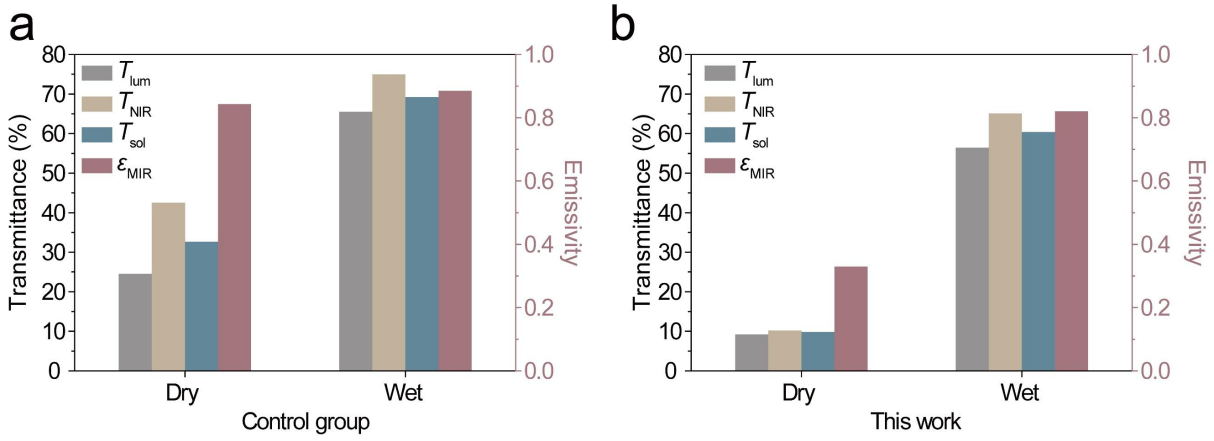

Figure S8. *Optical properties of (a) the control group and (b) the anticounterfeiting prototype under dry and wet states.*

Table S1. *Comparison of representative hydrochromic optical modulators reported in previous studies.*

Materials	Dry T_{lum}	Wet T_{lum}	ΔT_{lum}	$\Delta\varepsilon_{MIR}$
Porous PMMA (This work)	9.2%	56.4%	47.2%	0.55
Polyurethane/Polyethylenimine (PU/PEI)[9]	60%	88%	28%	-
Polyvinyl alcohol (PVA)-coated inverse opal polydimethylsiloxane (PDMS)[10]	14.18%	59.11%	44.93%	-
PMMA/water-chromic molecule oxazolidine (WMO) transparent wood[11]	84%	68%	16%	-
PVA/anthocyanin composite film[12]	78%	42%	36%	-
Poloxamer/ethyl cellulose-based polyurethane (PE-PU)[13]	~20%	~80%	~60%	-

Note: Values were extracted from the best reported optical transmittance in each study; when total luminous transmittance was unavailable, representative transmittance values reported in the original literature were used.

<References>

[1] Wyszecki, G. et al. *Color science: concepts and methods, quantitative data and formulae*, Wiley, Hoboken, NJ, **2000**.

[2] Astm, G. *ASTM International* **2003**.

[3] Inoue, T. et al. Realization of dynamic thermal emission control. *Nat. Mater.* **1 3**, 928–931 (2014).

[4] Wu, S.-H. et al. Thermal homeostasis using microstructured phase-change mater ials. *Optica* **4**, 1390–1396 (2017).

[5] Beadie, G. et al. Refractive index measurements of poly (methyl methacrylate) (PMMA) from 0.4–1.6 μm. *Appl. Opt.* **54**, F139–F143 (2015).

[6] Chaudhuri, T. K. & Patel, M. G. High refractive index films of ZnS/PVP nano composite by in situ thermolysis. *J. Exp. Nanosci.* **10**, 135–147 (2015).

[7] Tsuda, S. et al. Spectral and angular shaping of infrared radiation in a polymer resonator with molecular vibrational modes. *Opt. Express* **26**, 6899–6915 (201 8).

[8] Cleary, J. W. et al. Optical and electrical properties of ultra-thin indium tin oxi de nanofilms on silicon for infrared photonics. *Opt. Mater. Express* **8**, 1231–12 45 (2018).

[9] Si, P. et al. Nature-inspired robust hydrochromic film for dual anticounterfeitin g. *iScience* **24**, 102652 (2021).

[10] Yoo, G. Y. et al. Diphylleia grayi-inspired intelligent hydrochromic adhesive fil m. *ACS Appl. Mater. Interfaces* **12**, 49982–49991 (2020).

[11] Chen, Y. et al. Hydrochromic wood biocomposites for humidity and moisture d etection. *Chem. Eng. J.* **465**, 142890 (2023).

[12] Choi, J. & Hyun, J. Hydrochromic film for dynamic information storage using cellulose nanofibers and silica nanoparticles. *Carbohydr. Polym.* **327**, 121663 (2 024).

[13] Guo, Y., An, X. & Qian, X. Hydrochromic and piezochromic dual-responsive o ptical film derived from poloxamer and ethyl cellulose for visual fingerprints id entification. *Int. J. Biol. Macromol.* **270**, 132377 (2024).